REPORT DOCUMENTATION PAGE	AFRL-SR-AR-TR-05- 0027

Public reporting burden for this collection of information is estimated to average 1 hour per response, including ... gathering and maintaining the data needed, and completing and reviewing the collection of information. Send c ... collection of information, including suggestions for reducing this burden, to Washington Headquarters Services, ... Davis Highway, Suite 1204, Arlington, VA 22202-4302, and to the Office of Management and Budget, Paperwo ... Washington, DC 20503.

1. AGENCY USE ONLY *(Leave blank)*	2. REPORT DATE	3. REPORT TYPE AND DATES COVERED
		01 Oct 2002 - 31 Mar 2004 FINAL

4. TITLE AND SUBTITLE	5. FUNDING NUMBERS
LOW NOISE LARGE AREA AVALANCHE PHOTODIODES	000000 S181/19
6. AUTHOR(S) PROFESSOR CAMPBELL	
7. PERFORMING ORGANIZATION NAME(S) AND ADDRESS(ES) UNIVERSITY OF TEXAS AT AUSTIN 101 E 27TH STREET ROOM 4.308 AUSTIN TX 78712	8. PERFORMING ORGANIZATION REPORT NUMBER
9. SPONSORING/MONITORING AGENCY NAME(S) AND ADDRESS(ES) AFOSR/NE 4015 WILSON BLVD SUITE 713 ARLINGTON VA 22203	10. SPONSORING/MONITORING AGENCY REPORT NUMBER F49620-03-1-0001

11. SUPPLEMENTARY NOTES

12a. DISTRIBUTION AVAILABILITY STATEMENT	12b. DISTRIBUTION CODE
DISTRIBUTION STATEMENT A: Unlimited	

13. ABSTRACT *(Maximum 200 words)*

The goal of this program was to develop low-noise, large-area avalanche photodiodes (APDs) that operate at 1.55um. We successfully designed, fabricated, and characterized $In_{0.53}Ga_{0.47}As/In_{0.48}As$ avalanche photodiodes with diameters of 500um and 1mm. Six of these avalanche photodiodes were supplied to the contractor.

20050218 030

14. SUBJECT TERMS	15. NUMBER OF PAGES
	16. PRICE CODE

17. SECURITY CLASSIFICATION OF REPORT	18. SECURITY CLASSIFICATION OF THIS PAGE	19. SECURITY CLASSIFICATION OF ABSTRACT	20. LIMITATION OF ABSTRACT
Unclassified	Unclassified	Unclassified	UL

Low-Noise Large-Area Avalanche Photodiodes
F49620-03-1-0001

Final Report

Joe C. Campbell

Microelectronics Research Center

The University of Texas at Austin

UT/PRC/MER—R9950

Austin TX 78712

Telephone: (512) 471-9669

FAX: (512) 471-5625

jcc@mail.utexas.edu

DISTRIBUTION STATEMENT A
Approved for Public Release
Distribution Unlimited

Summary: The goal of this program was to develop low-noise, large-area avalanche photodiodes (APDs) that operate at 1.55μm. We successfully designed, fabricated, and characterized $In_{0.53}Ga_{0.47}As/In_{0.52}Al_{0.48}As$ avalanche photodiodes with diameters of 500μm and 1mm. Six of these avalanche photodiodes were supplied to the contractor.

Introduction

$In_{0.53}Ga_{0.47}As/In_{0.52}Al_{0.48}As$ avalanche photodiodes have been widely studied for optical communication applications. Most of the research efforts emphasized improving speed performance, in terms of gain-bandwidth product, by reducing device size in order to overcome the RC time limit and meet the strong demand of 10~40Gb/s system applications. However, optical measurement systems that operate in the eye-safety wavelength range (~1.5μm) require long-wavelength, high-sensitivity photodiodes with a large detection area.

All these requirements have created exciting challenges for epi-layer quality and device passivation in the InP-based material system. Large defect densities introduced during material growth (MBE or MOCVD) generate high bulk leakage current [1], severe micro-plasma-induced speed degradation [2], and poor device reliability for large-area APDs and arrays [3]. Sidewall passivation quality is critical to the APD dark current since sidewall leakage current constitutes a significant part of the total dark current, without proper passivation [4]. A 100μm-mesa-diameter InAlGaAs-InAlAs super-lattice APD integrated with a 200μm diameter microlens has been reported for eye-safety optical measurement purposes [5]. To the best of our knowledge, long-wavelength APDs with larger mesa area have not yet been reported.

In the following we describe large-mesa-area $In_{0.53}Ga_{0.47}As/In_{0.52}Al_{0.48}As$ long-wavelength APDs that exhibited high multiplication gains, high-gain bandwidth products, and low dark current densities. APDs with mesa diameters up to 500μm have demonstrated multiplied dark current densities $\leq 2.5\times10^{-2}$ nA/μm^2 at 90% of the breakdown. This large-area APD also exhibited a gain-bandwidth product >120 GHz. Origins of the dark current were analyzed based on the measured results, and primary dark current was dominated by the thermal-generation current induced by deep-level traps in the bulk $In_{0.53}Ga_{0.47}As$ absorber.

Device Structure Design and Material Growth

A separate absorption, charge, and multiplication (SACM) APD structure was utilized for the large-area device studies, since this type of device structure exhibits low dark current, low multiplication noise, and high speed if the device parameters are properly optimized. Fig. 1 shows the detailed device structure used for the large-area APD study.

The APD wafer was grown by molecular beam epitaxy on an *n*-type InP (100) substrate. The control over layer composition, thickness, and dopant density afforded by epitaxial growth allows several refinements in the APD design that are not possible to implement in homojunction APDs formed by standard dopant diffusion techniques. The low bandgap material necessary to receive the long-wavelength (1000–1700 nm) light is susceptible to

p+: InGaAs 9×10^{18}, 30nm
p+: InAlAs 9×10^{18}, 100nm
p+: InAlAs 7×10^{18}, 700nm
i: InAlAs spacer, 100nm
i: InGaAs,
i: InAlAs spacer, 100nm
p: InAlAs, 6×10^{17}, 150nm
i: InAlAs,
n+: InAlAs, 5×10^{18}, 100nm
n+: InAlAs, 5×10^{18}, buffer
n+:InP

Fig. 1 Device structure for the large-area APD study

leakage via inter-band tunneling when placed under strong bias. This source of dark current can be suppressed by isolating the low bandgap material in a dedicated absorption layer, in which the electric field is moderated by an adjacent charge layer. A second advantage of epitaxial growth is the ability to accurately control the epi-layer thickness in order to grow a thin multiplication

layer, so as to produce spatial modulation of impact ionization events, thereby suppressing multiplication noise [1,6]. However, these advanced designs typically involve multiplication layers on the order of 150 - 200 nm thick, supporting electric field strength above 700 kV/cm.

Consequently, small variations in epi-layer thickness caused by rough growth can have a large impact on device performance. In particular, premature breakdown can occur at thin spots in the multiplication layer, allowing excessive dark current to pass through the conductive micro-plasmas. Growth of smooth layers of uniform thickness is therefore essential.

Device Processing

Device processing began with *p*-type ohmic contact formation. A Cr (25 nm)/Au (85 nm) film was deposited by E-beam evaporation onto the heavily-doped $In_{0.53}Ga_{0.47}As$ cap layer. The contacts were patterned with standard photolithography and lift-off processing. A SiO_2 etch mask was then deposited by PECVD and mesa etch patterns were defined. The SiO_2 etch mask was used to ensure mesa pattern uniformity and smooth mesa edges. Mesas of different diameters (from 20μm to 500μm) were etched in phosphoric etchant (H_3PO_4:H_2O_2:H_2O = 1:1:8) to the n^+ InP buffer layer. After mesa etching, both the photoresist and the SiO_2 mask were removed. The wafer was quickly transferred to the PECVD chamber where a thin film of SiO_2 (~150 nm) was deposited for sidewall passivation. A Ni (20 nm)/AuGe (30 nm)/Au (80 nm) film was deposited by E-beam evaporation onto the InP buffer layer in order to form a common *n*-type ohmic contact.

Device Characterization and Discussions

Large-area InGaAs/InAlAs APDs

Most of the APDs exhibited relatively uniform I-V characteristics after processing. The punch-through voltage was ~15.0V, and the breakdown voltage was ~39.2V. The typical photoresponse and dark current curves of a 500μm-diameter APD are shown in Fig. 2.

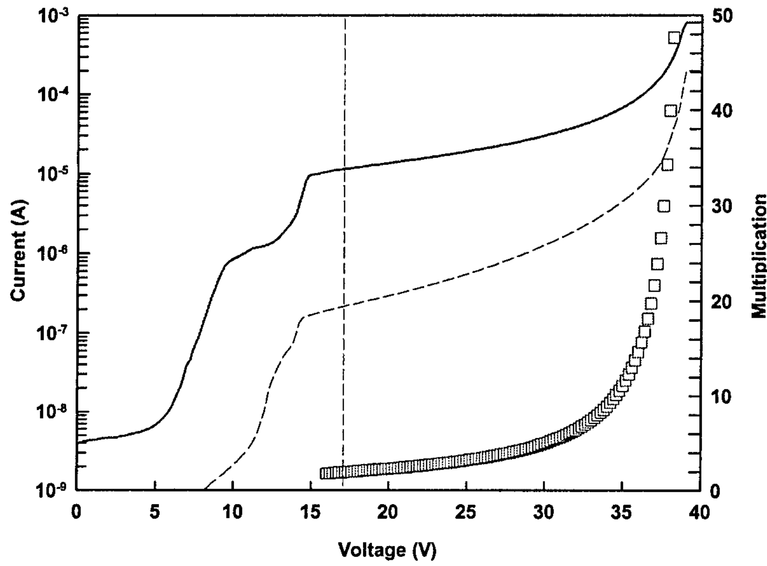

Fig. 2 Typical photo/dark current curve for a large-area (500μm diameter) APD

The photocurrent curve of the APD exhibited an obvious slope after punch-through, which might indicate multiplication gain at punch-through [1]. In order to characterize the multiplication gain, external quantum efficiencies were measured under different bias conditions above the punch-through voltage, using a tungsten-halogen light source, a spectrometer, and a lock-in amplifier. At a bias voltage of 16.0V, the APD was fully depleted and the measured

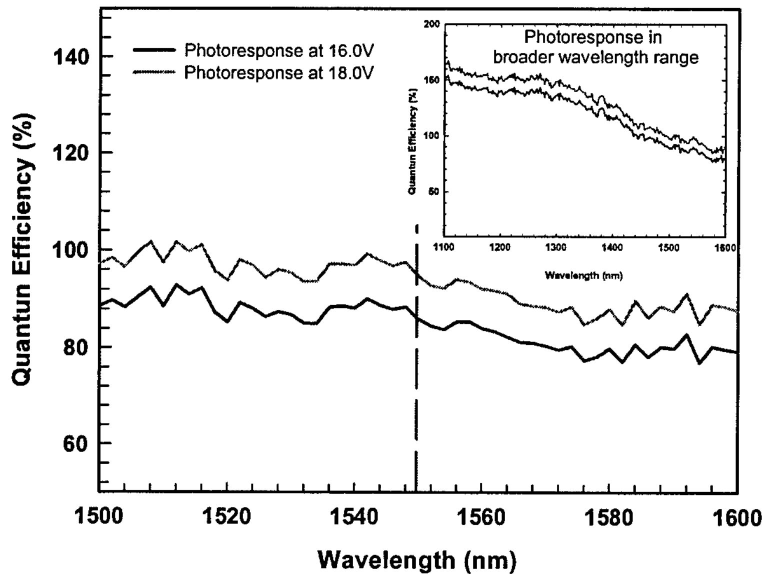

Fig. 3 Typical external quantum efficiency at a bias voltage of 16.0V and 18.0V

external quantum efficiency was ~85% at a wavelength of 1.55μm, as shown in Fig. 3. The expected external quantum efficiency of an APD at unity-gain can be estimated by the following expression:

$$\eta_{ext} = (1-R)\cdot(1-e^{-\alpha\cdot d})$$

where R is the reflection coefficient of the air-semiconductor interface; α is the absorption coefficient of $In_{0.53}Ga_{0.47}As$ at the relevant incident wavelength; and d is the absorption layer thickness. For a SACM APD, with a 1.5 μm-thick $In_{0.53}Ga_{0.47}As$ absorber that has an absorption coefficient (α) of 0.705 μm^{-1} at 1.55 μm [7,8], the expected external QE is ~46% at 1.55μm assuming an optical transmission of 70% (R=0.3) at the air-semiconductor interface. The measured value (~85%) is 1.8 times higher than the expected quantum efficiency value (~46%). We attribute this large quantum efficiency to the gain at punch-through, and the gain at a bias voltage of 16.0V is calculated as 1.8, without overestimation. The assertion of multiplication gain at punch-through can also be corroborated by electric field strength analysis. At a reverse bias voltage of 16.0V, the electric field in the $In_{0.52}Al_{0.48}As$ multiplication region can be estimated as ~580kV/cm using the simple depletion approximation, assuming a 200nm $In_{0.52}Al_{0.48}As$ un-doped multiplication region and a 150nm p-type (6×10^{17} cm^{-3}) $In_{0.52}Al_{0.48}As$ charge region. This calculated value of electric field strength agrees well with the published homo-junction APD result [9], from which the electric field strength in the 200nm-thick multiplication region of an $In_{0.52}Al_{0.48}As$ APD at a gain of 1.8 can be inferred as ~560KV/cm.

The gain of the APD was then calculated using the following expression:

$$M^* = \frac{I_p - I_d}{I_{pu} - I_{du}}, \quad M = M_0 \cdot M^*$$

where M_0 is the gain factor determined by a quantum efficiency measurement at the specific reference bias voltage after punch-through (e.g. 16.0V). I_p and I_d are the photocurrent and dark current for bias values above the reference voltage; I_{pu} and I_{du} are the primary photocurrent and dark current at the reference voltage. M^* is the gain from the I-V measurement and M is the final

calculated gain of the APD. The calculated gain curve of a 500μm-diameter APD was plotted in Fig. 2, and all the APDs with mesa diameters ranging from 20μm to 500μm exhibited gain values greater than 40, at a reasonably low dark current level.

APD Surface Leakage Current

Even though thin multiplication region avalanche photodiodes provide low multiplication noise and high gain-bandwidth products due to non-local impact ionization effects, the APD dark current is a very critical performance parameter. This due to the fact that the gain is increased until the APD noise is comparable to that of the following circuitry. Consequently, the dark current is a determining factor in the signal to noise ratio.

Previously, dark current studies of SACM APDs primarily focused on sidewall passivation quality and various device passivation techniques, such as sidewall passivation using PECVD deposited SiN_x films [10] and SiO_2 films [3], polymide-based materials [11], and even BCB-based materials [3], to achieve low surface leakage current density. Even though recently published results have shown that the surface leakage current, if properly passivated, could be negligible in comparison to bulk material related dark current [3], the nature of this bulk-related dark current was not very clear.

To examine the dark current dependence on surface passivation, dark currents of APDs with different mesa sizes were characterized at room temperature with a HP 4145B semiconductor parameter analyzer, as shown in Fig. 4. The dark current of the 30μm-diameter APD was compared to previous results [3,10,11]. The value of the measured dark current at a bias voltage of 35.2V (90% of breakdown, gain >10) was ~26.7nA, which is much less than that of the SiN_x-passivated APDs (0.7μA/30μm by Kagawa et al, 0.41μA/30μm by Kim et al, and 0.4μA/80μm by Makita et al), the polyimide-passivated APDs (67nA/30μm by Kim et al), or the BCB-passivated APDs (38nA/30μm reported by Kim et al).

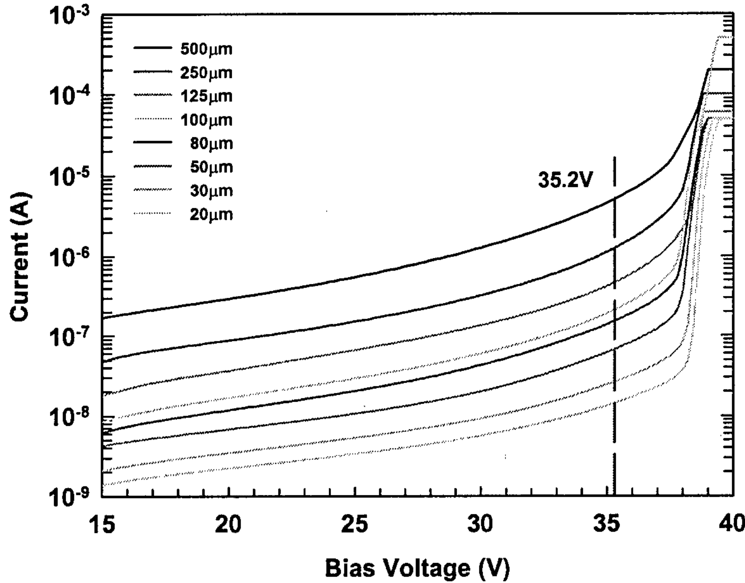

Fig. 4 Typical dark current curves from APDs of various diameters

The APD dark current can be divided into two categories by the leakage path: the bulk leakage current, which is proportional to the mesa area, and the sidewall leakage current, which is only proportional to the mesa perimeter, neglecting the mesa sidewall curvature caused by wet etching. The total dark current can be expressed as:

$$I_{total} = J_{sidewall} \cdot \pi \cdot d + \frac{J_{bulk} \cdot \pi \cdot d^2}{4}$$

where $J_{sidewall}$ is the sidewall leakage current density (A/m), and J_{bulk} is the bulk leakage current density (A/m^2). The measured dark currents were fitted to the mesa diameter using a quadratic fit at a bias voltage of ~35.2V (90% of the breakdown), as shown in Fig. 5.

An almost perfect quadratic fit was achieved, thus the bulk leakage current was found to be dominant for large area devices. The fitted surface dark current density $J_{sidewall}$ was 0.19nA/μm, and the bulk dark current density was 0.023 nA/μm^2 at 90% of the breakdown voltage. The dark current can be also divided into two components by the multiplication

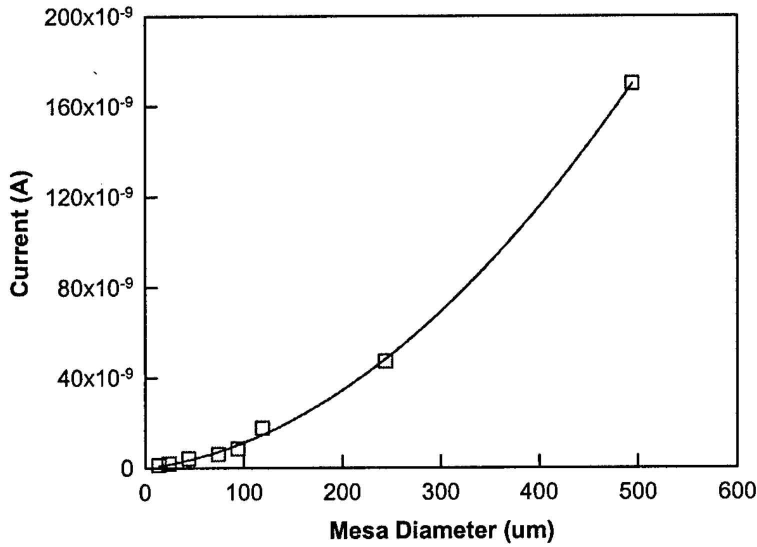

Fig. 5 Dark current as a function of the device diameter, at a bias of 16.0V

mechanism: the multiplied dark current that flows through the bulk and the un-multiplied dark current that normally flows through the mesa sidewall, as expressed in the following equation:

$$I_{total} = I_{un-multiplied} + I_{multiplied} \cdot M$$

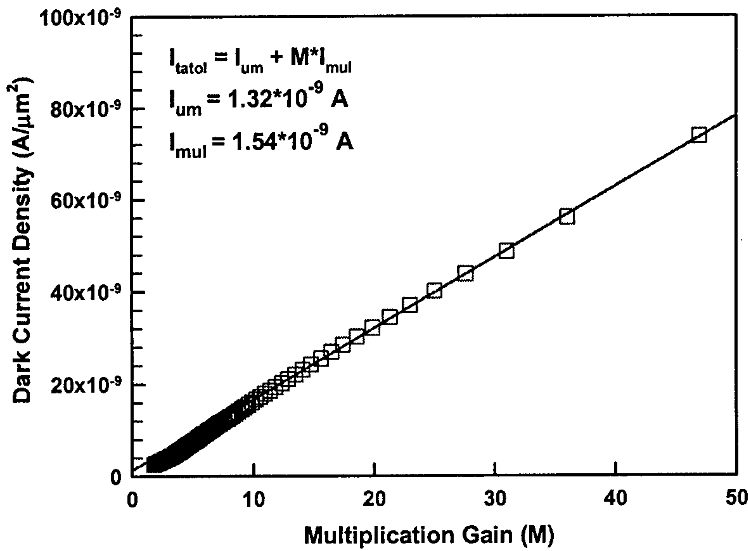

Fig. 6 APD dark current as a function of the multiplication gain

The dark current of a 100μm-diameter APD was fitted with the above equation, as shown in Fig. 6. The un-multiplied dark current (density) was ~1.32nA (4.2pA/μm) and the multiplied dark current was ~1.54nA. The dependence of dark current on gain remains linear even at gains of 50. The un-multiplied dark current (density) is rather small compared to the multiplied dark current component and is negligible for APDs biased at high gains.

The spatial photoresponse profile of the large-mesa-area APD was measured by the raster-scanning technique. A 1.5-μm-wavelength He-Ne laser beam with a beam-waist <5um was scanned across a 500μm-diameter APD at a bias voltage of 36.8V (gain≥20). A flat, uniform photoresponse profile was obtained across the entire device mesa area, as shown in Fig. 7. No obvious photoresponse peak was found around the mesa edge at high gains, which indicates that the electric field strength at the mesa edge is not approximately equal to that in the mesa bulk region, thus no strong evidence of edge-breakdown has been observed.

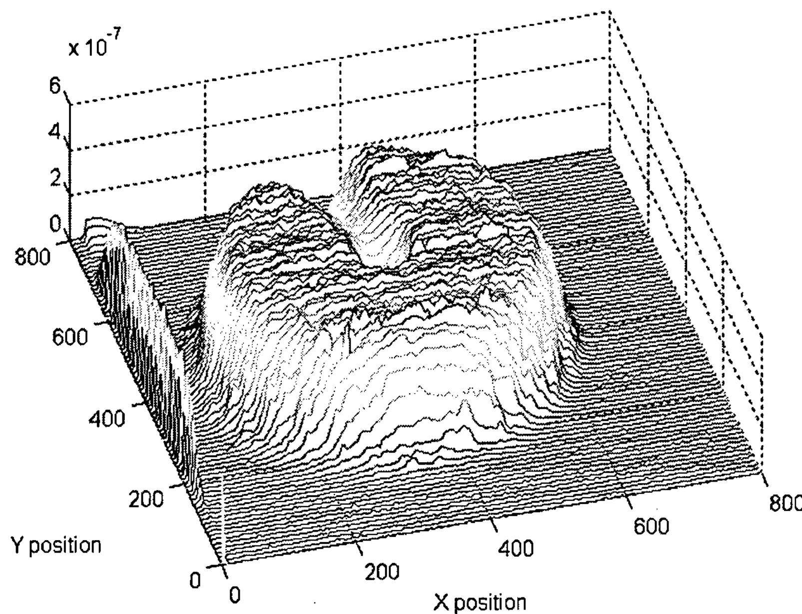

Fig. 7 Spatial distribution of the photoresponse, by 2-D raster scanning

Dark Current Dependence on Surface Morphology

Dark current dependence on surface morphology was also examined using SACM APD structures, in collaboration with A. Hungtinton, et al, at UCSB. The SACM APD wafer design was based on the considerations discussed in previous chapters. Several $In_{0.53}Ga_{0.47}As/In_{0.52}Al_{0.48}As$ SACM APD wafers, in which three variants of multiplication layer thickness were utilized, were grown and categorized by wafer surface morphology conditions. Five of the resulting wafers were selected for the morphology study. These five wafers, labeled #1 to #5, cover the full range of morphology conditions. Detailed information about each wafer is listed in Table 1.

Sample	M-layer Thickness ( )	Defect Density (cm^{-2})	Roughness ΔZ/RMS ( )	Dominant Morphological Feature
#1 (021029D)	2000	150	99.3/10.5	-
#2 (021029C)	2000	200	392.9/48.6	Moderate μ-roughness
#3 (021028A)	2000	200	461.5/70.6	Severe μ-roughness
#4 (021029E)	1500	4,000	255.9/44.0	loading dust
#5 (021028B)	1500	> 10,000	415.4/51.9	desorption defects

Table 1 Surface morphology of SACM APD wafers, after MBE growth

Defect density, as listed in the second column, was estimated by visual inspection of defect counts on the wafer surface, using a Nomarski microscope. Defect assignments were obtained through a combination of inference based on variations in growth conditions and direct inspection via AFM, as illustrated in Fig. 8 (a) through (c).

From surface morphology observations, at a growth temperature of 500°C, optimal surface conditions were obtained from sample #1, which was grown under 8×10^{-6} Torr of arsenic pressure, as shown in Fig. 8 (a). However, a metal-rich polycrystalline surface, was obtained from using a lower arsenic pressure (4×10^{-6} Torr) (Fig. 8(b)), and significant three-dimensional

islanding was observed using a higher arsenic pressure (1.2×10^{-5} Torr) (Fig. 8(c)).

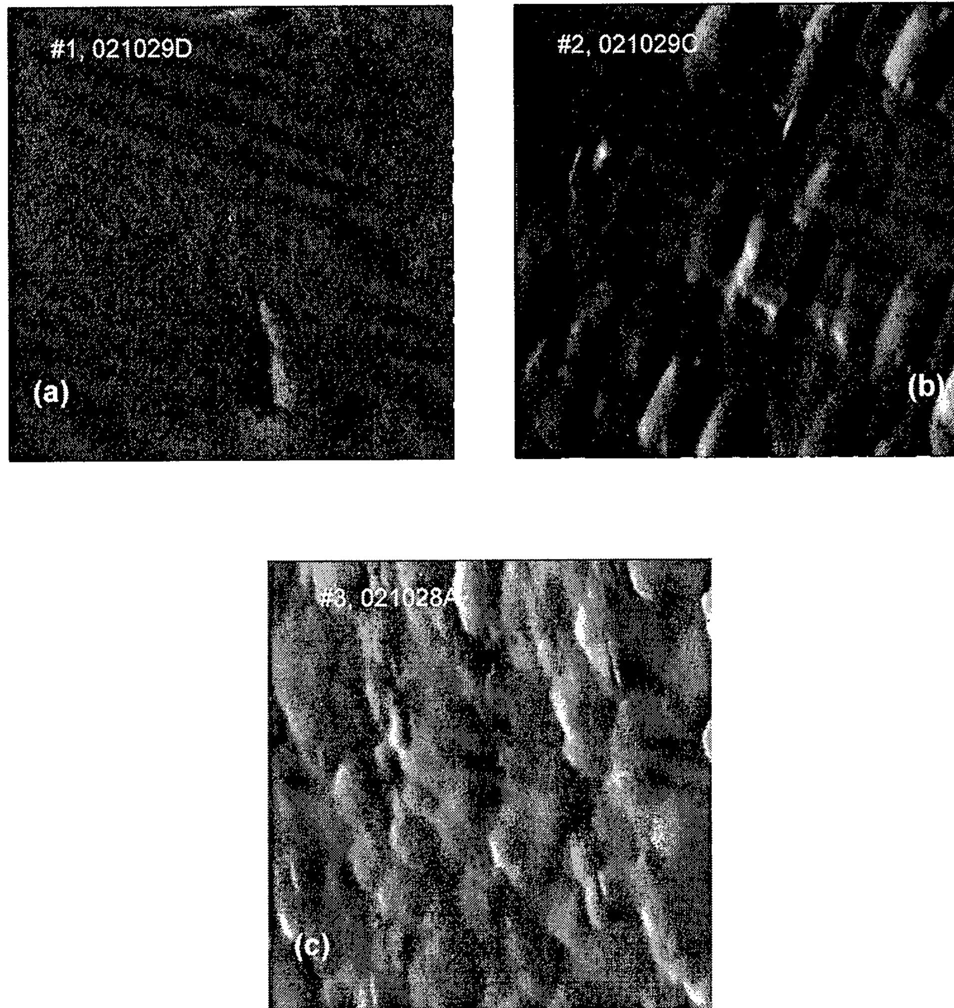

Fig. 8 Illustration of various morphology conditions of SACM APD wafers, (a) 021029D, (b) 021029C, (c) 021028A

Devices obtained from five wafer samples were carefully measured to quantify the relationship between surface roughness and leakage (dark) current, and devices from all these wafers were grouped into three different sets to characterize APD dark current properties.

Wafer #1, #2, and #3 were included in the first device set, in which the APD multiplication region thickness was similar (200nm) but the wafer surface morphology was different. Devices with a moderate mesa diameter (125μm) were used to represent typical APD behaviors, since the mesa size is large enough to include enough defects, if present. The

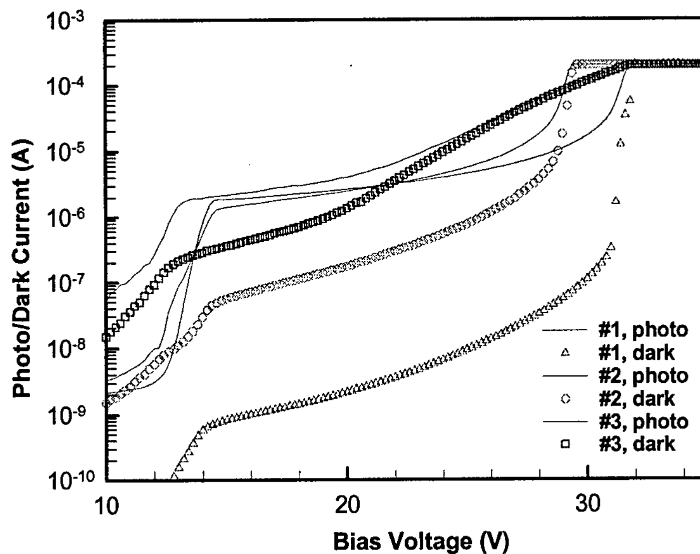

Fig. 9 Dark current dependence on surface roughness of SACM APD wafers

qualitative relationship between surface roughness and leakage current can be found in Fig. 9. In ascending order, samples #1, #2, and #3 cover the entire roughness range in this study. It is quite clear from this observation that surface roughness is strongly correlated to dark current levels.

So far, only the impact of roughness on the dark current characteristics of devices from wafers with different surface morphologies has been compared. A complete study of surface roughness requires an understanding of how the wafer surface condition causes device performance variation across a single wafer. Thus, 15 devices each from wafers #4, #2, and #5 were measured in order to investigate performance uniformity. For this study, the 125μm diameter devices were selected to exclude gross defects, in order to isolate the effects of surface

roughness.

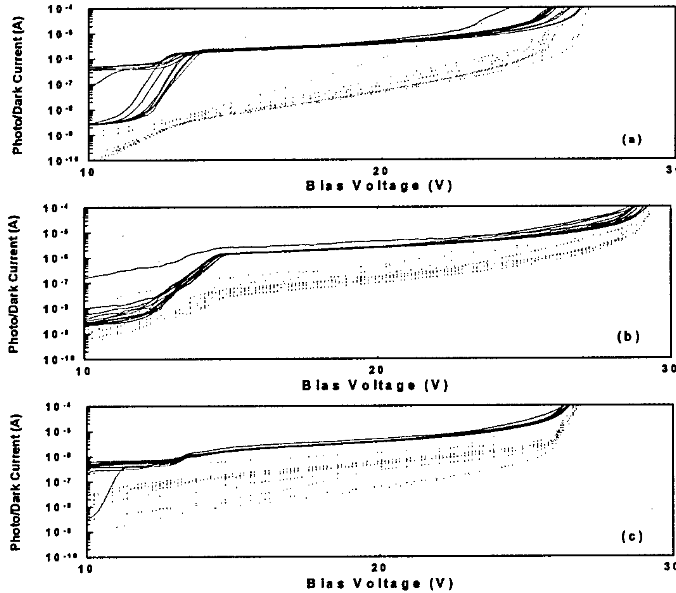

Fig. 10 I-V characteristics of 15 devices, from wafer (a) #4, (b) #2, and (c) #5.

It appears that, in addition to the degraded mean dark current value, large variations in surface roughness also increase the spread in the dark current distribution across an entire wafer, as shown in Fig. 10 The observation that I-V characteristics become more scattered for rougher wafers is further strengthened by the previous APD array study. Although those APD focal-plane array results did not directly address the issue of roughness, the APD array in question was fabricated from a relatively smoother wafer (similar to sample #1), and the standard deviation of the dark current at punch-through was ~10%, a fraction of the mean value, compared to 42% for sample #4, 61% for sample #2, and 90% for sample #5, as tabulated in table 2.

Table 2 Surface morphology impacts on device variation in a SACM APD wafer

Sample	RMS Roughness (´)	$\langle I_{dark} \rangle$ at M = 1	σIdark	$\frac{\sigma_{Idark}}{\langle I_{dark} \rangle}$
Array	~ 10.5	2.00 nA	0.19 nA	9.5%
#4	44.0	9.38 nA	3.96 nA	42.2%
#2	48.6	53.57 nA	32.47 nA	60.61%
#5	51.9	191.18 nA	172.88 nA	90.43%

A third set of 250μm-diameter devices, 30 devices in each group from wafers #2, #4, and #5, were examined to observe the affects of defects, originating from either dust or a bad desorption procedure, on device performance. Devices with larger diameters were also investigated in order to potentially include more defects generated from either the initial substrate, further material growth, or the final device processing steps. The 250 μm devices from the data set had a large enough area and were measured in sufficient numbers to provide a range of how the two types of defects affect final device yield. All three wafers suffer to varying degrees from surface roughness, but beyond this, two distinct failure mechanisms are apparent in the I-V characteristics, as shown in Fig. 11.

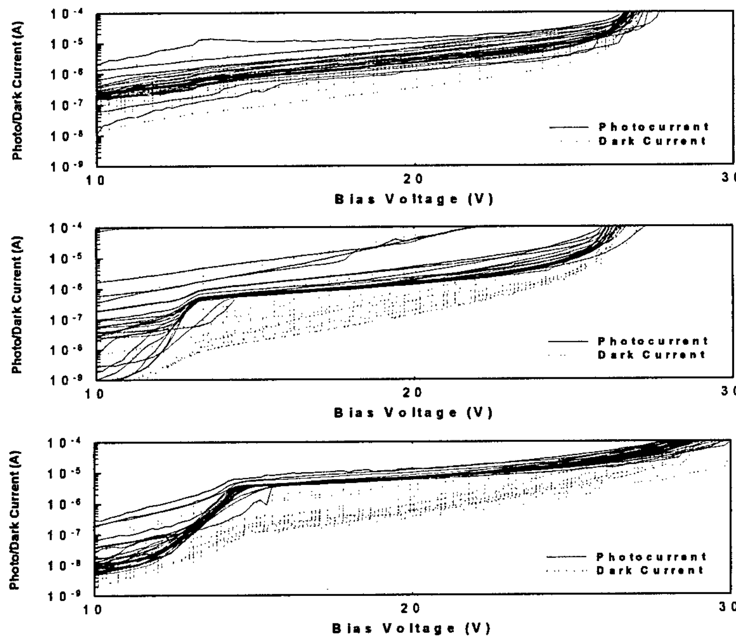

Fig. 11 DC characteristics of samples #2 (top), #4 (middle), and #5 (bottom).

Sample #4, which had the highest density of dust-related defects, produced a number of devices that failed to behave like photodiodes. These devices pass high current at low voltage and are insensitive to illumination, which are essentially caused by shorts. Sample #5 has at least one short in it, while the great majority of its devices have photodiode-like I-V characteristics, but with extremely high dark current. This behavior, characterized by preservation of the basic

APD I-V curve shape but with excessive leakage, is similar to that associated with extreme roughness.

The failure mechanisms associated with the two different types of defects can be attributed to their structural differences. As revealed by AFM, cratering caused by dust tends to pierce the entire epitaxial structure, creating an alternative current leakage path that shorts the entire APD structure. That is why dust-related failures do not preserve the basic shape of an APD I-V characteristic. On the other hand, desorption defects look more like a patch of hyper-roughness under the AFM. It seems plausible that they would have an analogous effect upon device performance. Fortunately, the influence of these defects is limited only to their immediate area. Functional devices can be obtained from wafers with a relatively high defect density by fabricating small-diameter devices.

In summary, precise control of the growth conditions that create surface is extremely critical in the growth of good quality SACM APD wafers, especially for those with very thin multiplication layers (e.g. <200-nm). In APDs with thick multiplication layers, surface roughness will result in relatively minor variations in electric field strength over the area of the thick multiplication region. When the peak-to-peak roughness of epi-layers approaches similar dimensions to the multiplication layer, it might become the deciding factor in the final device characteristic, particularly for a high-speed focal-plane APD array with a thin multiplication region.

Modeling of InGaAs/InAlAs APD Dark Currents

APD dark current has been a big issue for both InGaAs-InAlAs APD design and fabrication. If too high, the dark current will degrade the achievable APD sensitivity by increasing minimum detectable signal level at high gains. Based on previous experimental results, a preliminary picture of APD dark current was developed, as shown in Fig. 12, in which APD dark current mechanisms are illustrated.

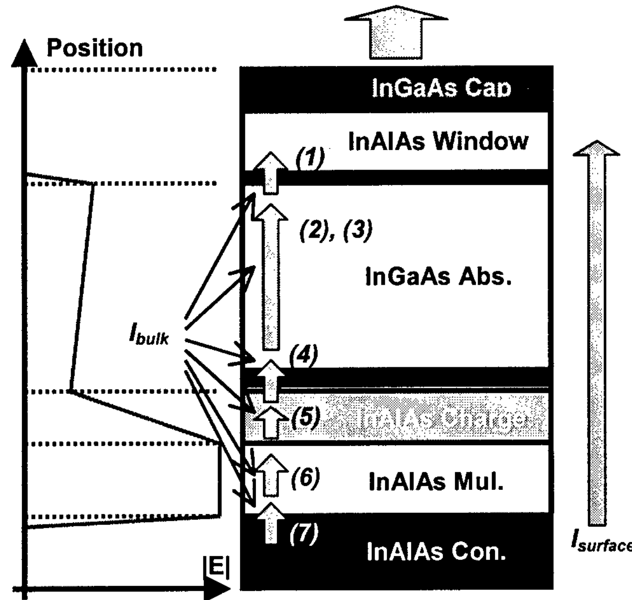

Fig. 8.12 Possible dark current sources of an InGaAs/InAlAs SACM APD

Theoretically, the main contribution to the APD dark current comes from thermal generation in the depleted intrinsic region. At room temperature, a dark current density of ~ 10^{-7}A/cm^2 would be expected from an InGaAs-InAlAs APD, if only band-to-band thermal generation is considered. Practically, however, a dark current density of ~10^{-5}A/cm^2 is usually observed. A bump close to the punch-through voltage on the dark current curve is always observed at room temperature, as shown in Fig. 13. This may be a clue to isolating the exact source(s) of the observed excess dark current density.

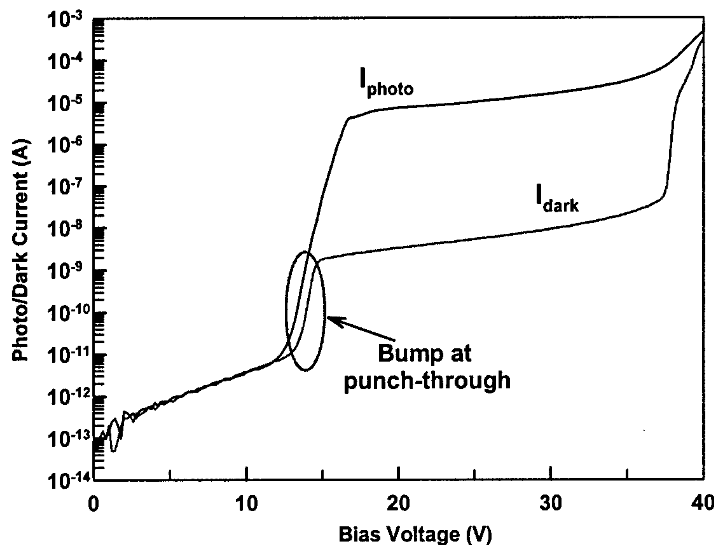

Fig. 13 Bump on the dark current curve of an InGaAs/InAlAs SACM APD

Dark current originates from various sources, as categorized in equation (8.8), which can be found in many semiconductor textbooks

$$I_{d,tot}(T) = I_{diff}(T) + I_{thermal-gen}(T) + I_{bulk-trap}(T) + I_{interface-trap}(T) + I_{surface}(T) + I_{tunneling}(T) + I_{defect}(T) + \ldots\ldots$$

In this equation, all dark current components are functions of ambient temperature, and they all have distinguishing signatures as a function of temperature. Diffusion currents $I_{diff}(T)$, or more precisely, reverse generation currents, which exist in the heavily-doped, neutral *p*- and *n*-InAlAs contact regions (region 1 and 7 in Fig. 12), constitute a negligible component of the total APD dark current. Tunneling current $I_{tunneling}(T)$, either in the narrow bandgap InGaAs absorption region (regions 2 and 3) or in the thin InAlAs multiplication region (region 6), is a minor dark current source if the electric field profile in the APD is optimized. Also, since tunneling current has a specific exponential signature, it can be easily identified if it exists. The surface leakage, if the device is not passivated well, may comprise a large component of the total dark current. Proper device passivation, either using silicon dioxide or BCB polymers, could reduce the leakage current to an insignificant contribution. Defects, either by dust or improper desorption, could also generate large dark current levels in an APD. With optimized growth conditions and proper device processing, obtaining a defect-free device is quite feasible.

Trap-assisted thermal generation might be responsible for the bump on the dark current curve. To verify this, APD dark current was measured at elevated temperatures (25°C to 150°C) to observe the dependence on ambient temperature. Here elevated temperature is preferred over low temperature because incomplete dopant ionization at low temperatures might occur, which would decrease the total charge amount in the charge layer. As a result, at a fixed bias above punch-through, the APD gain increases as does the multiplied dark current. Temperature induced gain variation at a fixed bias voltage complicates experimental data acquisition and further data analysis. At a moderate elevated temperature less than 200°C, the APD gain at punch-through remains nearly constant. The measured APD dark current as a function of the temperature is

plotted in Fig. 14.

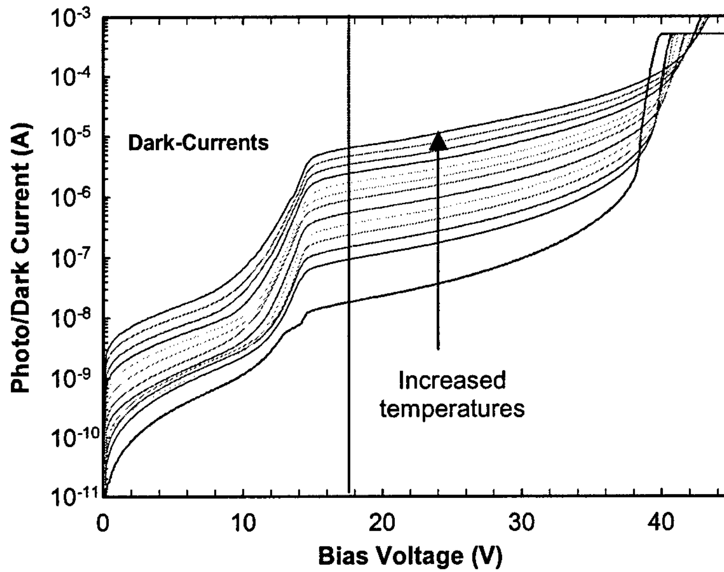

Fig. 14. Dark current temperature dependence of InGaAs/InAlAs SACM APDs

The temperature dependence of the APD dark current demonstrated that the logarithm of the dark current densities were proportional to the inverse temperature, as shown in Fig. 15. As temperature increases, higher thermal generation rates, which are exponentially dependent on the

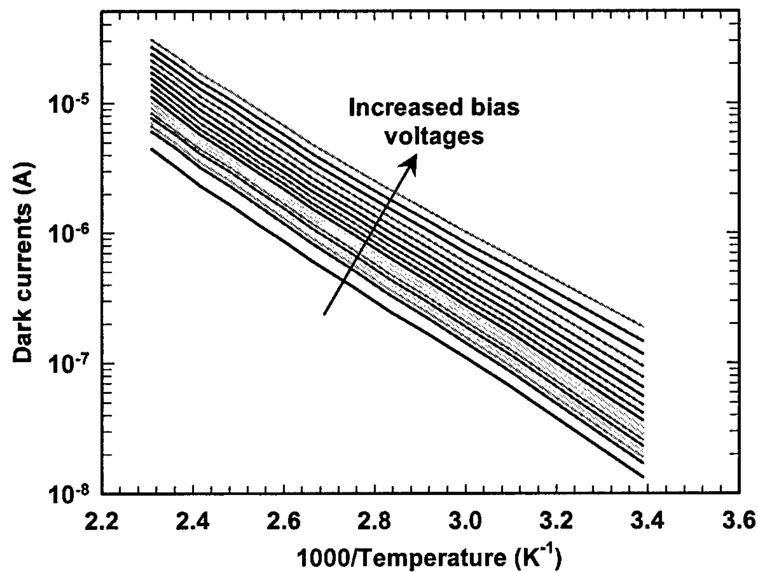

Fig. 15 InGaAs/InAlAs APD dark current as a function of 1000/T

ambient temperature, cause higher dark current levels. Further fitting of the extracted data from the temperature measurements was done using a thermal emission current model, which indicated that the APD dark currents primarily originated from thermal generation originated. The extracted average activation energy of traps, which might be generated during MBE growth, was approximately ~0.45eV.

To better understand the origin of the bulk leakage current, a new set of SACM APD structures were fabricated. These APD structures have the same multiplication layer thickness (200 nm) but different absorption layer thickness, 1.0μm (sample A), 1.3μm(sample B), and 1.5μm (sample C). In these wafers, digital alloy transition layers were also incorporated in InAlAs-InGaAs interfaces to smooth carrier transport across the hetero-junction. The electric field in the multiplication region in these devices was similar at punch-through. Two other samples, one with a 1.3μm-thick absorber (sample D) and another with a 1.5μm-thick absorber

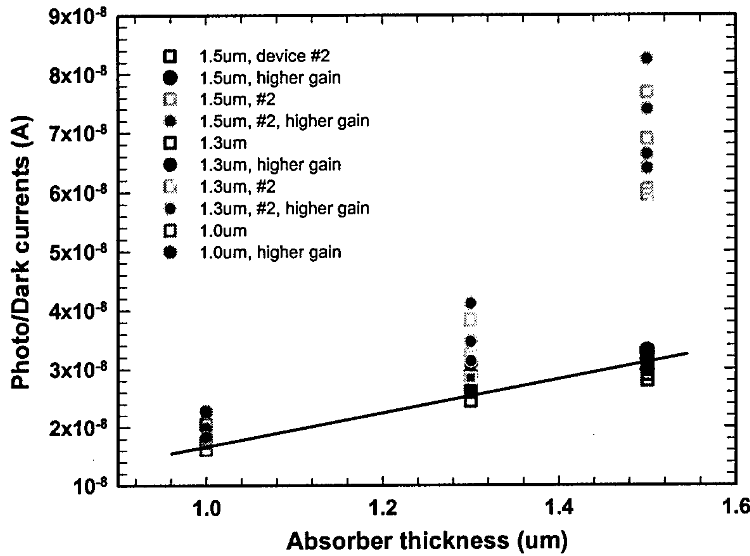

Fig. 16 InGaAs/InAlAs APD Dark current dependence on absorber thickness

(sample E), were also grown as reference wafers for samples A through C, but without incorporating digital alloy transition layers. All these samples were grown in growth runs close to each other, in order to obtain the most consistent epi-layer quality among wafers. Simple mesa

devices were processed using conditions discussed previously, and the dark currents were measured from those devices at room temperature. A nearly linear relation between the dark current density and the InGaAs absorber thickness, as shown in Fig. 16, was observed from three different wafers. Devices from the other two wafers exhibited excessive dark current densities, probably due to inferior wafer quality. This result indicated that trap-induced thermal generation currents, from which the main constituent of the total InGaAs/InAlAs APD dark current was comprised, are bulk-related in the $In_{0.53}Ga_{0.47}As$ absorption region.

Summary

Large-area $In_{0.53}Ga_{0.47}As/In_{0.52}Al_{0.48}As$ APDs with a mesa diameter of 500μm, have been demonstrated at room temperature. These devices exhibited a very low dark current density of $\sim 2.5\times10^{-2} nA/\mu m^2$ at 90% of breakdown. Very low surface leakage current density (~4.2pA/μm) was achieved with wet chemical etching and SiO_2 passivation. Further investigation and analysis of the dark current has shown that, APD bulk leakage current, which is a dominant part of the total APD dark current, originates from the thermal generation assisted by deep-level traps in the $In_{0.53}Ga_{0.47}As$ absorber.

References:

249

[1] G. S. Kinsey, J. C. Campbell, and A. G. Dentai, "Waveguide avalanche photodiode with a gain-bandwidth product of 320 GHz", IEEE Photonics Technology Letters, Vol. 13, Issue 8, 842-844, August 2001

[2] Geoff S. Kinsey, "Waveguide Avalanche Photodetectors," Ph.D. Dessertation, The University of Texas at Austin, Chapter 8, p. 36.

[3] H.S. Kim, J.H. Choi, H.M. Bang, Y. Jee, S.W. Yun, J. Burm, M.D. Kim, and A.G. Choo, "Dark current reduction in APD with BCB passivation", Electronics Letters, pp 455-457, *29*,Vol. 37, no. 7, March 2001

[4] D. Schmidt and D. Trommer, "Conservation of low dark current of InGaAs photodiodes after NH_3F/HF etch a BCB passivation layer", Indium Phosphide and Related Materials, 2000 Conference Proceedings, Page 302 -305

[5] M. Hayashi, I. Wantababe, T. Nakata, M. Tsuji, K. Makita, S. Yamakata, and K. Taguchi, "Microlens-Integrated Large-Area InAlGaAs-InAlAs Superlattice APD's for Eye-Safety 1.5-μm Wavelength Optical Measurement Use", IEEE Photonics Technology Letters, pp 576-578 Vol. 10, no. 4, April 1998

[6] Lenox, C., Nie, H., Yuan, P., Kinsey, G., Holmes Jr., A. L., Streetman, B. G., and Campbell, J. C. "Resonant-Cavity InGaAs-InAlAs avalanche photodiodes with gain-bandwidth product of 290 GHz," *IEEE Photon. Technol. Lett.*, 1999, vol. 11, no. 9, pp. 1162-1164

[7] Humphreys, D. A., King, R. J.: 'Measurement of absorption coefficients of $Ga_{0.47}In_{0.53}As$ over the wavelength range 1.0-1.7μm', *Electron. Lett.*, 1985, vol. 21, no. 25/26, pp. 1187-1189

[8] Bacher, F. R., Blakemore, J. S., Ebner, J. T., Arthur, J. R.: 'Optical-absorption coefficient of $In_{1-x}Ga_xAs/InP$', *Phys. Rev. B*, 1988, vol. 37, no. 5, pp.2551-25

[9] Lenox, C., Yuan, P., Nie, H., Baklenov, O., Hansing, C., Campbell, J. C., Holmes Jr., A. L., Streetman, B. G.: 'Thin multiplication region InAlAs homojunction avalanche photodiodes', *Appl. Phys. Lett.*, 1998, vol. 73, no. 6, pp. 783-784

[10] Kagawa, T., Kawamura, Y., and Iwamura, H., 'A wide-bandwidth low-noise InGaAsP-InAlAs superlattice avalanche photodiode with a flip-chip structure for wavelength of 1.3μm and 1.55μm', IEEE J. Quantum Electron., 1993, **29**, pp 1387-1392

[11] Makita, K., Watanabe, I., Tsuji, M., and Taguchi, K., "Dark current and breakdown analysis in In(Al)GaAs/InAlAs superlattice avalanche photodiodes", Jpn. J. Appl. Phys., 1996, 35, pp. 3440-3444

Listing

Refereed journal papers and conference proceedings

1. X. G. Zheng, J. Hsu, et al., "Long-wavelength InGaAs/InAlAs Large-area APDs and Arrays", J. Quantum Electron., vol. 40, no. 8, pp. 1068-1073 (2004).
2. X. G. Zheng, J. Hsu, X. Sun, J. B. Hurst, X. Li, S. Wang, A.L. Holmes, Jr., J. C. Campbell, "A 12 x 12 $In_{0.53}Ga_{0.47}As/In_{0.52}Al_{0.48}As$ avalanche photodiode array," IEEE J. Quant. Elec., vol. 38, no. 11, pp. 1536-40, Nov. 2002.

3. Joe C. Campbell, Shuling Wang, X. G. Zheng, G. S. Kinsey, A. L. Holmes, Jr., X. Sun, R. Sidhu, and P. Yuan, "Ultra-low-noise avalanche photodiodes," Proc. SPIE, vol. 4283, pp.480-488, 2001
4. Xiaowei Li, Xiaoguang Zheng, Shuling Wang, Feng Ma, J.C. Campbell, "Calculation of gain and noise with dead space for GaAs and $Al_xGa_{1-x}As$ avalanche photodiode", IEEE Transactions on Electron Devices, Vol.49 No.7, pp. 1112 –1117, Jul. 2002
5. S. Wang, F. Ma, X. Li, R. Sidhu, X. G. Zheng, X. Sun, A. L. Holmes, Jr., and J. C. Campbell, "Ultra-low noise avalanche photodiodes with a 'centered-well' multiplication region," IEEE J. Quan. Elec., vol. 39, no. 2, pp.375-378, Feb. 2003.
6. S. Wang, J. B. Hurst, F. Ma, R. Sidhu, X. Sun, X. G. Zheng, A. L. Holmes, Jr., J. C. Campbell, A. Huntington, and L. A. Coldren, "Low-noise impact-ionization engineered avalanche photodiodes grown on InP substrate," IEEE Photonics Tech. Lett., vol. 14, no. 12, pp. 1722-24, 2002.
7. S. Wang, R. Sidhu, G. Karve, F. Ma, X. Li, X. G. Zheng, J. B. Hurst, X. Sun, N. Li, A. L. Holmes, Jr., and J. C. Campbell, "A study of low-bias photocurrent gradient of avalanche photodiodes," IEEE Trans. Elect. Dev., vol. 49, no. 12, pp. 2107-2113, Dec. 2002.
8. F. Ma, S. Wang, X. Li, K. A. Anselm, X. G. Zheng, A. L. Holmes, Jr., and J. C. Campbell, "Monte Carlo simulation of low-noise avalanche photodiodes with heterojunctions," J. Appl. Phys., vol. 92, no. 8, pp. 4791-5, Oct. 2002.
9. S. Wang, R. Sidhu, X.G. Zheng, X. Sun, A.L. Holmes, Jr., and J. C. Campbell, "Low noise avalanche photodiodes with a graded Impact-Ionization-Engineered multiplication region," IEEE Photonics Technology Letters, vol. 13, no. 12, pp.1346- 8, 2001
10. N. Li, R. Sidhu, X. Li, F. Ma, X. Zheng, S. Wang, G. Karve, S. Demiguel, A. L. Holmes, Jr., and J. C. Campbell, "InGaAs/InAlAs Avalanche Photodiode with Undepleted Absorber," Appl. Phys. Lett., Vol. 82 No.13, pp2175-2177, Mar. 2003

International Conferences

1. X. G. Zheng, J. Hsu, X. Sun, J. B. Hurst, X. Li, S. Wang, A.L. Holmes Jr., J. C. Campbell, "A 12 × 12 InGaAs/InAlAs Avalanche Photodetector Array", OSA/IPR Conference, 2002.
2. J. B. Hurst, X. G. Zheng, X. Sun, S. Wang, Joe C. Campbell, and Archie L. Holmes, Jr., "Long wavelength InGaAs/InAlAs/InP-GaAs/AlGaAs avalanche photodiode implemented by direct wafer bonding," 2002 Electronic Materials Conference, Santa Barbara, California, June, 2002.
3. S. Wang, R. Sidhu, X.G. Zheng, X. Sun, A.L. Holmes, Jr., and J. C. Campbell, "Low noise avalanche photodiodes with a graded Impact-Ionization-Engineered multiplication region", 59th Annual Device Research Conference, Latest news.
4. S. Wang, X. Sun, X. G. Zheng, A. L. Holmes, J. C. Campbell, and P. Yuan, "Avalanche photodiodes with an impact-ionization-engineered multiplication region," Lasers and Electro-Optics Society 2000 Annual Meeting, 13th Annual Meeting, Vol.1, Page(s): 9 – 10, 2000.
5. S. Wang, J. B. Hurst, F. Ma, R. Sidhu, X. G. Zheng, A. L. Holmes, Jr., J. C. Campbell, A. Huntington, and L. A. Coldren, "Low-noise InP-based avalanche photodiodes with an impact-ionization-engineered multiplication region," 2002 IEEE/LEOS Annual Meeting Conf. Proc., Glasgow, Scotland, pp. 488-489.

Deliverables

Below are the I-V characteristics of the 500μm- and 1mm-diameter $In_{0.53}Ga_{0.47}As/In_{0.52}Al_{0.48}As$ avalanche photodiodes that were supplied to the contractor.

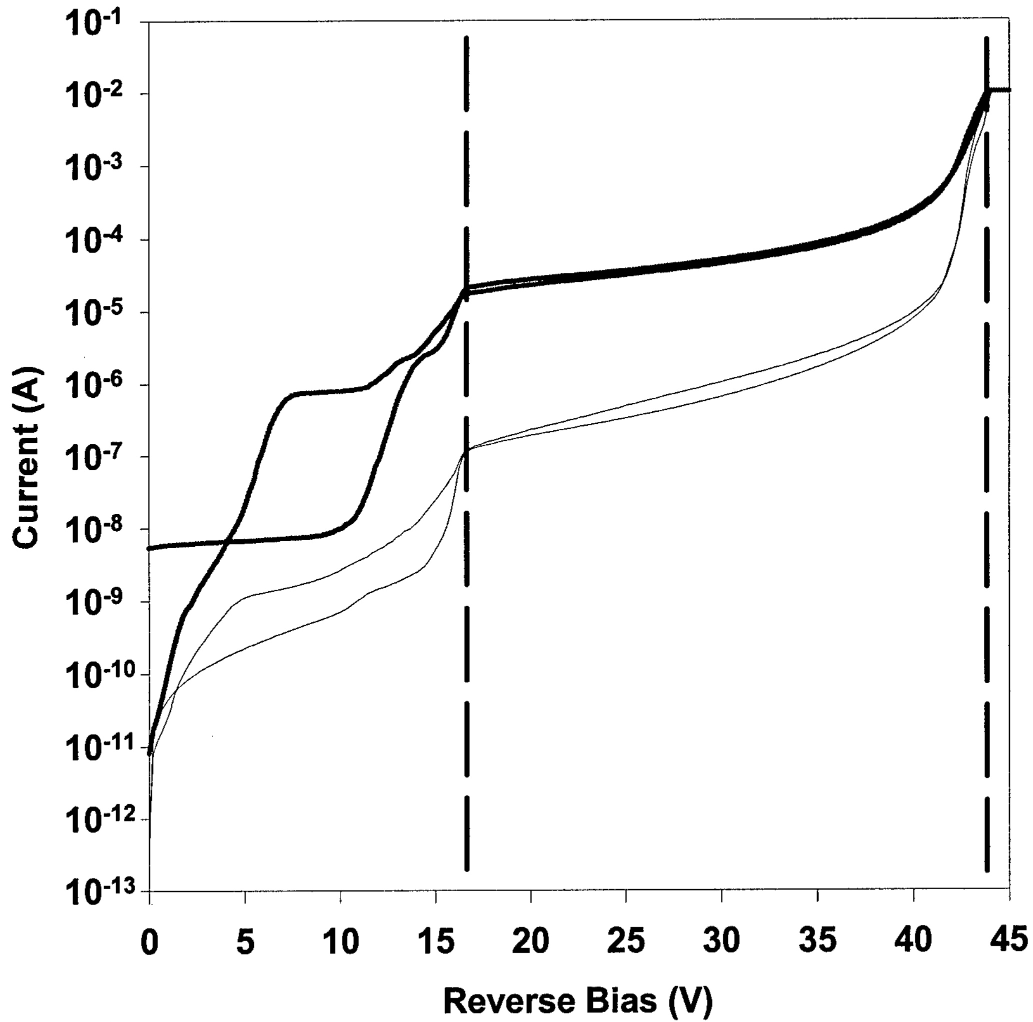

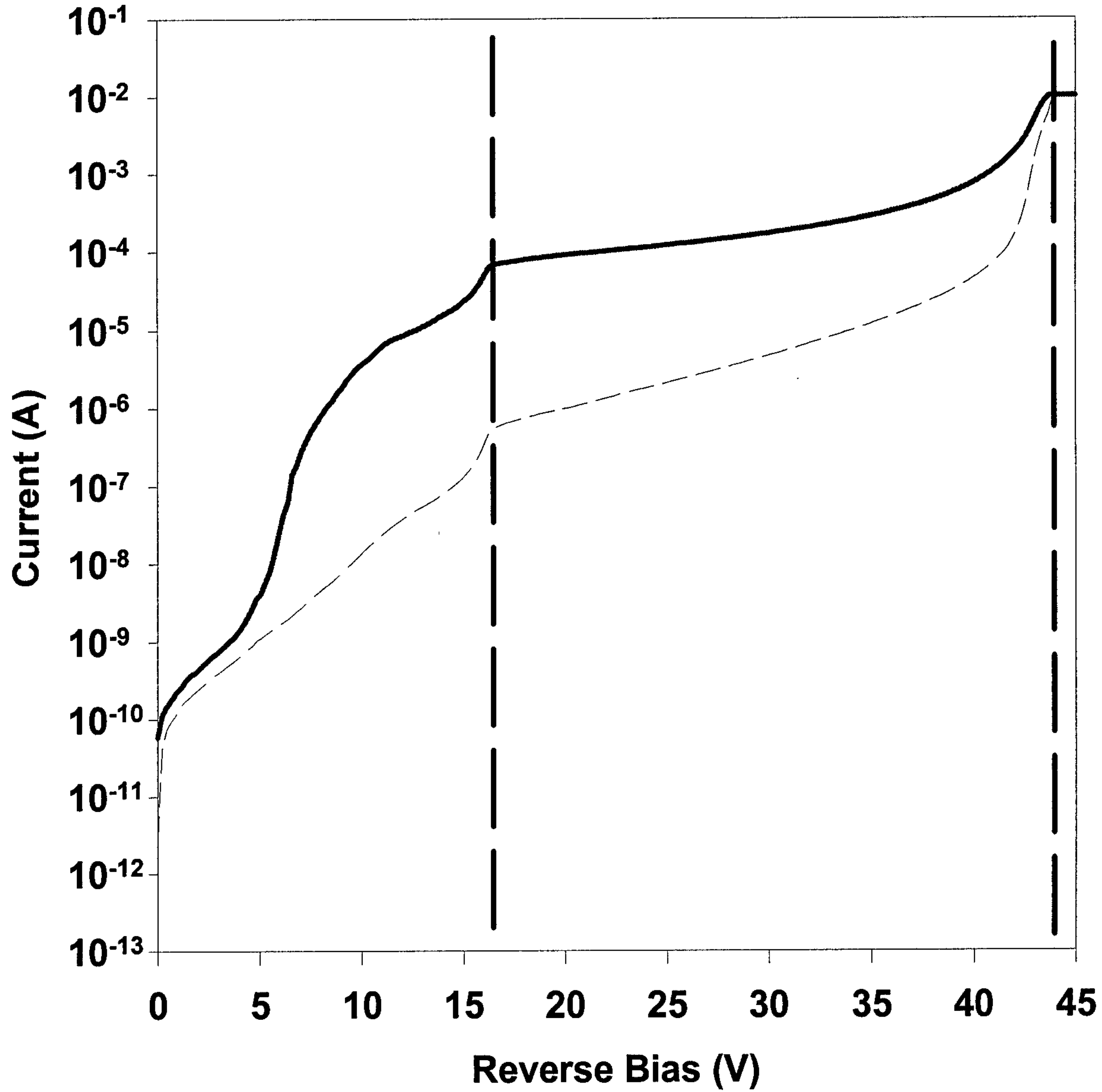

Typical I-V of a 1mm diameter APD
Current (A)
10-1
10-2
10-3
10-4
10-5
10-6
10-7
10-8
10-9
10-10
10-11
10-12
10-13
0
5
10
15
20
25
30
35
40
45
Reverse Bias (V)